

Interaction potentials for fast atoms in front of Al surfaces probed by rainbow scattering

P. Tiwald,¹ A. Schüller,² H. Winter,² K. Tökesi,³ F. Aigner,¹ S. Gräfe,¹ C. Lemell,¹ and J. Burgdörfer¹

¹*Institute for Theoretical Physics, Vienna University of Technology, Wiedner Hauptstraße 8-10, A-1040 Vienna, Austria, EU*

²*Institut für Physik, Humboldt-Universität zu Berlin, Newtonstr. 15, D-12489 Berlin-Adlershof, Germany, EU*

³*Institute of Nuclear Research of the Hungarian Academy of Sciences (ATOMKI), P.O. Box 51, H-4001 Debrecen, Hungary, EU*

(Received 11 June 2010; published 29 September 2010)

Rainbow scattering for grazing-angle incidence of atoms at surfaces along low-indexed channeling directions provides a sensitive probe of quasistatic atom-surface potentials. The dependence of the rainbow angle on the kinetic energy for the projectile motion perpendicular to the surface, E_{\perp} , varies with the electronic structure of the projectile as well as the crystallographic face of the aluminum surface. Comparison between experiment and classical Monte Carlo trajectory simulations demonstrates that the superposition of binary atom-atom potentials fails to adequately represent the equipotential surfaces. *Ab initio* atom-surface potentials based on density-functional theory are required to reach satisfactory agreement with experiment.

DOI: [10.1103/PhysRevB.82.125453](https://doi.org/10.1103/PhysRevB.82.125453)

PACS number(s): 79.20.Rf, 34.20.Cf, 34.35.+a

I. INTRODUCTION

Scattering of atoms off solid surfaces has developed into a versatile tool for the investigations of surface structure, of nonadiabatic dynamical processes, and of quantum diffraction effects. As early as 1929, Stern and collaborators demonstrated the wave nature of hyperthermal He atoms diffracting off alkali-halide surfaces.¹ Thermal energy atom scattering²⁻⁴ is nowadays employed to accurately probe properties of surfaces. At higher collision energies, grazing-angle incidence of atoms allows one to probe surface potentials at relatively large distances in soft collisions.⁵

For small incidence angles ($\phi_{in} \approx 1^\circ$) the interaction is characterized by widely disparate kinetic energies parallel ($E_{\parallel} = E_0 \cos^2 \phi_{in} \approx E_0$) and normal ($E_{\perp} = E_0 \sin^2 \phi_{in} \approx E_0 \phi_{in}^2$) to the surface [Fig. 1(a)]. The fast motion along the surface results in a weak coupling between the longitudinal and the transverse degrees of freedom.⁶ By averaging the atom-surface potential along the direction of the incident atom (y direction), the scattered particle experiences an effective two-dimensional (2D) atomic string potential $V_{str}(x, z)$ along well-defined channels.⁷ For very low perpendicular energies ($E_{\perp} \lesssim 1$ eV) quantum diffraction has been observed^{8,9} despite the high energy $E_{\parallel} (\gtrsim 1$ keV) parallel to the surface. This is due to the vastly different projected de Broglie wavelengths

$$\lambda_{dB\perp, \parallel} = 2\pi/k_{\perp, \parallel} = 2\pi\hbar/\sqrt{2ME_{\perp, \parallel}}, \quad (1)$$

where $k_{\parallel} = k_y$ and $k_{\perp} = k_z$ are parallel and normal components of the wave vector of the incident beam, respectively. While $\lambda_{dB\perp}$ is comparable to the lattice spacing, $\lambda_{dB\parallel}$ is orders of magnitude smaller. One consequence of the approximate separability of longitudinal and transverse motion is the effective suppression of decoherence¹⁰ which is key to the visibility of quantum interferences at kiloelectron volt total energies E_0 .

For somewhat larger perpendicular $E_{\perp} (\gtrsim 10$ eV), quantum effects are expected to be of minor importance and a classical-trajectory description of channeling to be valid. Only then rainbow scattering at low-indexed surface channels can be used as a *local* probe of surface potentials. The

disparate energy and velocity scales for parallel and perpendicular motions have also a decisive impact on the validity and applicability of various approximations to atom-surface potentials. While the perpendicular energy E_{\perp} controls the distance of closest approach and thus the isopotential lines to be probed, the parallel energy E_{\parallel} , or more precisely, the velocity component parallel to the surface v_{\parallel} determines whether quasistatic interaction potentials¹¹ apply or the dynamical response has to be accounted for. For small $v_{\parallel} \ll v_e$ (v_e : characteristic speed of the electronic motion such as the Fermi velocity v_F for metals or orbital velocity v_{orb} of the valence electrons in atoms) quasistatic (or zero-frequency) potentials $V(\vec{r}) = V(\omega=0, \vec{r})$ are expected to be valid while at larger velocities nonadiabatic effects will set in. The present investigation focuses on quasistatic interaction potentials for Al as a prototypical metal surface. We show that the frequently employed superposition of binary atom-atom potentials is inadequate for representing channeling potentials in the quasistatic limit. The position of the critical angle for rainbow scattering, θ_{rb} , is shown to be a sensitive tool for probing atom-surface potentials in a regime where quantum corrections to classical rainbow scattering can be neglected and the quasistatic limit still applies. Only *ab initio* calculations for potential surfaces of the combined “quasimolecular” system of atom plus aluminum surface are capable of reproducing the dependence of θ_{rb} on the (perpendicular) energy E_{\perp} for different surface channels on different faces of Al and different types of atomic projectiles. For atoms with a high-electron affinity the breakdown of the static quasimolecular potential approximation is observed at higher parallel velocities.

II. CHANNELING AND RAINBOW SCATTERING

We consider scattering of neutral atoms off aluminum surfaces under grazing angles of incidence of $\phi_{in} \approx 1^\circ$ and $E_{\perp} \ll E_{\parallel}$. The perpendicular energy is assumed to be sufficiently large ($E_{\perp} > 1$ eV) such that quantum diffraction effects can be ignored (see below). The parallel velocity in our experiment was large enough to allow for classical simulations of channeling trajectories ($E_{\parallel} \gg E_{\perp}$) yet sufficiently slow (v_{\parallel}

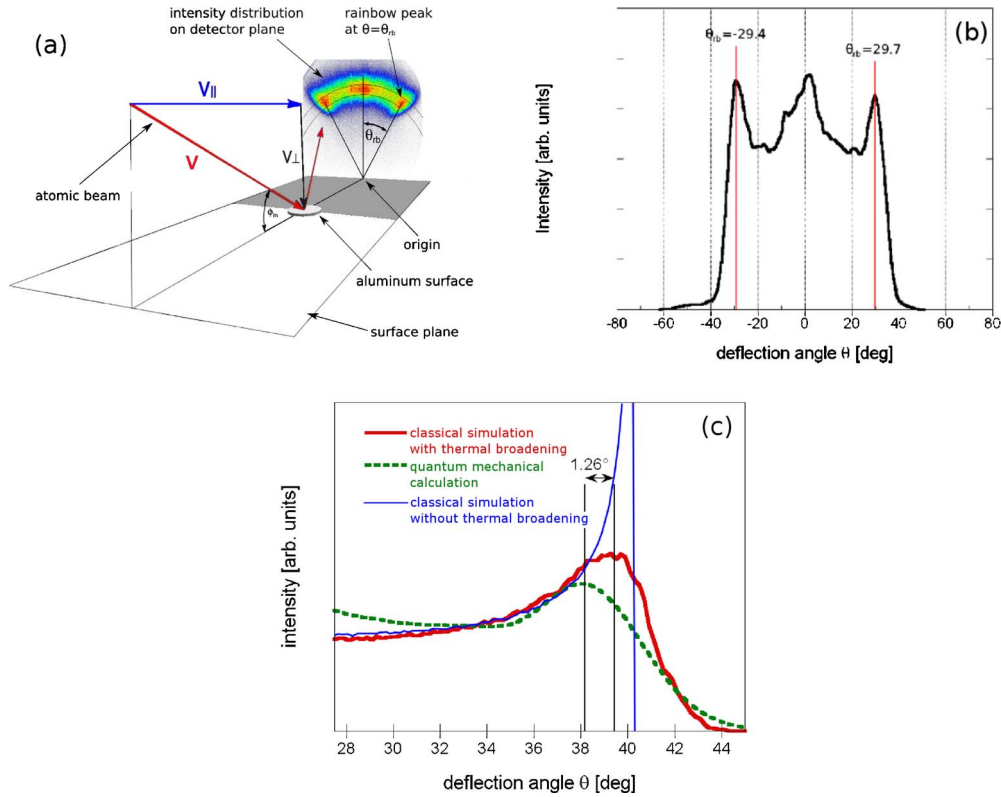


FIG. 1. (Color online) (a) Schematic picture of the scattering geometry. The 2D intensity distribution on the detector plane arises from scattering of 10 keV Ar atoms from Al(111) along a $\langle 1\bar{1}0 \rangle$ direction at angle of incidence $\phi_{in}=2.35^\circ$. This corresponds to an energy perpendicular to the surface of $E_{\perp}=16.81$ eV. Positions of rainbow angles θ_{rb} are indicated by straight lines. Color code: red to blue (=high to low). (b) Integral over the 2D intensity within the two concentric circles along fixed values of θ . The two concentric circles represent the region of (elastically) scattered projectiles. (c) Angular distributions calculated with CTMC simulations and matter-wave simulations (for details see Ref. 10), both including thermal lattice vibrations, for He scattered off an Al(111) surface along the $\langle 1\bar{1}0 \rangle$ direction with $E_{\perp}=9$ eV. The thin blue line indicates the classical result without thermal broadening.

$\ll v_e$) that adiabatic, quasistatic potential surfaces govern these trajectories.

Scattering from the surface proceeds in the regime of “surface channeling” by averaged interaction potentials.^{7,11} The axial channeling or string potential is given by

$$V_{str}(x,z) = \frac{1}{\Delta y} \int_{y_0}^{y_0+\Delta y} dy V(x,y,z), \quad (2)$$

where the y coordinate is aligned along a low-indexed channeling direction ($\sim \hat{v}_{\parallel}$) of the Al crystal, x is the transverse coordinate in the surface plane while the z coordinate points in outward normal direction. The distance Δy is the period of string potential along a given channeling direction (on the order of the lattice constant a). Similarly, the planar channeling potential is given by

$$V_{planar}(z) = \frac{1}{\Delta A} \int_{unit\ cell} dx dy V(x,y,z) \quad (3)$$

with ΔA the area of the surface unit cell. The string potential $V_{str}(x,z)$ gives rise to rainbow scattering.^{4,12} Classically, whenever the deflection function $\theta(x)$, where x is the “impact parameter” or, as in the present case, the coordinate perpendicular to the channel, has an extremum $d\theta/dx=0$ within the

open interval $-\pi/2 < \theta < \pi/2$, the differential cross section, $\sigma(\theta_{rb}) = |dx/d\theta(\theta_{rb})|$ possesses a first-order singularity at the rainbow angle $\theta = \theta_{rb}$. Finite beam divergence, energy dispersion, thermal broadening, surface imperfections, and detection resolution convert the singularity into a peak of finite height and width [Fig. 1(b)]. Moreover, even in the absence of any such convolution, quantum diffraction due to the locally increased de Broglie wavelength near the caustic broadens and slightly shifts the rainbow peak [Fig. 1(c)].

In our simulations we perform classical-trajectory Monte Carlo (CTMC) calculations using the Runge-Kutta method for the transport of atomic projectiles through channels of various faces of atomically flat Al surfaces. Beam parameters (energy, direction, and divergence) were chosen to match the experiment. Initial starting positions are uniformly distributed over the channel, i.e., the x coordinate. The final angular distribution is extracted from the receding trajectory recorded at a distance $z=8$ a.u. above the surface. In order to probe for quantum diffraction effects we have performed sample quantum wave-packet simulations¹⁰ employing identical string potentials. A comparison between θ distributions [Fig. 1(c)] calculated with classical trajectory and matter wave calculations for He atoms scattered off an Al(111) surface along the $\langle 1\bar{1}0 \rangle$ direction including thermal lattice vibrations clearly shows that the difference in angle between

the classical and quantum (first-order) rainbow peaks is well below the angular resolution in the experiment. Therefore, the classical value θ_{rb} can be compared with the experiment without a significant error. Rainbow angles from trajectory simulations based on channeling potentials differ hardly from results of three-dimensional molecular-dynamics simulations as shown in Ref. 13. Furthermore, as thermal lattice vibrations broaden the rainbow peaks but hardly alter their position,^{13,14} θ_{rb} can be extracted neglecting thermal effects [thin blue line in Fig. 1(c)]. A typical angular distribution recorded in the experiment is shown in Fig. 1(a) for scattering of an $E_0=10$ keV argon beam off an Al(111) surface along the $\langle 1\bar{1}0 \rangle$ direction (i.e., \vec{v}_{\parallel} is parallel to the $\langle 1\bar{1}0 \rangle$ direction). The intensity distribution reflects the axial symmetry for scattering along atomic strings under axial surface channeling conditions. The two intensity maxima at the edge of the distribution represent the rainbow peaks located at the rainbow angle θ_{rb} , the angle in the detector plane relative to the vertical line through the intersection of the beam axis with the surface plane [Fig. 1(a)]. The annulus in the detector plane represents elastically scattered projectiles. The integral of the 2D intensity within this annulus [Fig. 1(b)] shows three peaks including the rainbow peaks at angles $\theta = \pm \theta_{rb}$. Their dependence on total energy $E_0 \approx E_{\parallel}$, perpendicular energy E_{\perp} , projectile species, and crystallographic orientation of the Al surface will be investigated experimentally and theoretically in the following.

III. EXPERIMENT

A. Setup

Beams of atoms with total kinetic energies $E_0 = m_p \cdot v^2/2$ ranging from 2 to 100 keV are scattered off single-crystal Al(111), Al(001), and Al(110) surfaces at room temperature under grazing angles of incidence $0.4^\circ < \phi_{in} < 2^\circ$. The azimuthal orientation of the beams is parallel to a low-indexed crystal direction in the surface plane. After scattering off the surface the projectiles are recorded by a position-sensitive multichannelplate detector.

The surfaces were prepared by cycles of sputtering with 25 keV Ar⁺ ions under grazing incidence of typically 2° and subsequent annealing to temperatures of about 500°C . Ion beams were produced in a 10 GHz electron cyclotron resonance (ECR) ion source (Nanogan Pantechnique, Caen, France). For N, O, and rare-gas ions the source was operated with pure gases, and for S and F ions with SF₆ gas. Na and Cl ions were produced via evaporation of NaCl in an Ar plasma of the ECR source. Al ions were generated by sputtering of an Al wire, Fe, Cr by sputtering of a stainless-steel screw in an Ar plasma of the ECR source. Li, K, and Cs ions were produced by beta-eucryptit sources (HeatWaveLabs Inc.). In order to keep the target surface clean, the experiments were performed under UHV conditions. A base pressure of 5×10^{-11} mbar was reached in our UHV chamber by a turbomolecular pump in series with a titanium sublimation pump, where the pressure gradient with respect to the beam line of the accelerator (5×10^{-7} mbar) was maintained by two differential pumping stages. Pairs of slits separating

these stages were used for the collimation of the incident beam to a divergence of $< 0.03^\circ$.

In order to avoid effects of the image charge on projectile trajectories present for ions,⁵ neutral atoms are selected on the incoming as well as the outgoing paths. Atomic projectiles were produced by neutralization of ions in a gas cell mounted in the beamline of the accelerator operated with rare gases or Cs vapor. Remaining ions were deflected by an electric field. The charge state of scattered projectiles was checked using electric-field plates between target and detector. Angular distributions for scattered projectiles were recorded by means of a position-sensitive multichannelplate detector with a delay-line anode (DLD40, Roentdek Handels GmbH) located 66 cm behind the target. At typical count rates of some 10^4 counts/s, the low dose of impinging atoms did not cause noticeable effects of radiation damage on the target surface during the measurements.

B. Experimental results

The dependence of the rainbow angle θ_{rb} on the energy component normal to the surface plane $E_{\perp} = m_p \cdot v_{\perp}^2/2 = E_0 \sin^2 \phi_{in}$ strongly varies with atomic species as shown in Fig. 2. Rare gases [Fig. 2(a)] serve as benchmark relative to which open shell atoms are analyzed [Figs. 2(b)–2(e)]. Starting at a finite threshold value for rainbow scattering $E_{\perp}^{rb} \approx 2$ eV, θ_{rb} monotonically increases with normal energy E_{\perp} with the slope depending on the atomic number of the projectile. θ_{rb} is independent of the total energy E_0 at constant E_{\perp} with the exception of He scattered off Al(111) along the $\langle 1\bar{1}0 \rangle$ direction as discussed below. The monotonic increase in θ_{rb} with E_{\perp} was observed for all rare-gas atoms and all channeling directions of different Al faces. For metal atoms, in particular alkali atoms [Figs. 2(b) and 2(c)], $\theta_{rb}(E_{\perp})$ features a minimum whose position depends on the atomic species. At low perpendicular energies E_{\perp} an increase in θ_{rb} is observed. While the dependence of θ_{rb} on E_{\perp} is completely different for low normal energies, for larger E_{\perp} , θ_{rb} approaches those of rare-gas projectiles with comparable nuclear charge. Note that also for this group of projectiles, θ_{rb} is independent of E_0 or E_{\parallel} at fixed E_{\perp} [the fit to the rare-gas data (Ar) is displayed in panels c and d for comparison].

Finally, for atoms with large electron affinities such as halides (from fluorine up to bromine), N, O, and S θ_{rb} depends at small E_{\perp} on the total projectile energy E_0 , whereas for larger E_{\perp} this dependence becomes weak. As showcases for this group, the rainbow angles for S and Cl projectiles are plotted in Figs. 2(d) and 2(e). For low E_0 , θ_{rb} increases with decreasing E_{\perp} as observed for alkali and metal projectiles but shows a rare-gaslike behavior for larger E_0 . The different behavior for these three groups of atoms is ascribed to species-dependent interactions between the atoms and the metal surface.

IV. CALCULATION OF CHANNELING POTENTIALS

A. Binary pair potentials

The remarkably different behavior of θ_{rb} for different groups of atomic projectiles points to the strong dependence

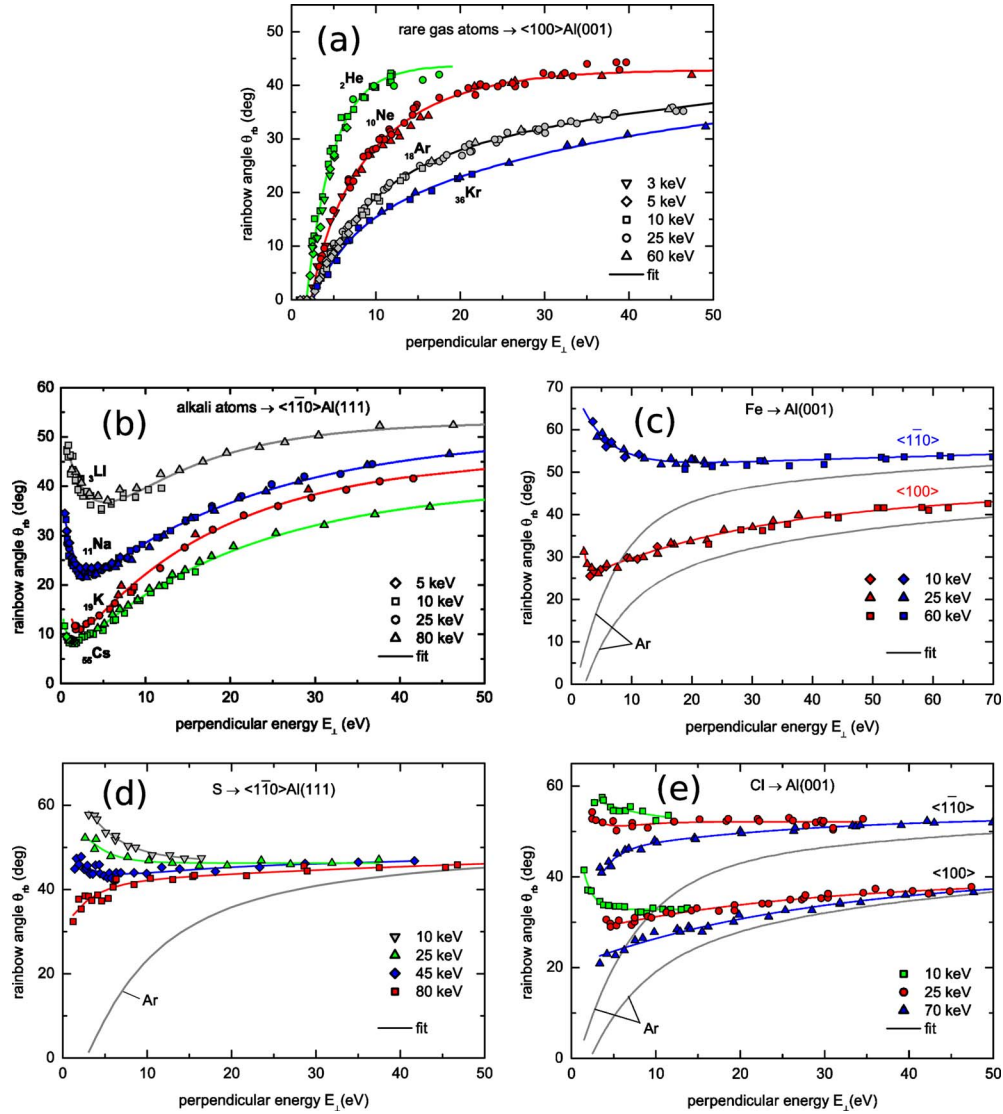


FIG. 2. (Color online) Experimentally observed rainbow angles θ_{rb} as function of normal component of kinetic energy of projectiles E_{\perp} for scattering of (a) rare gases, [(b) and (c)] metal atoms (alkali and Fe), and the high-affinity atoms (d) S and (e) Cl from Al surfaces along low-indexed directions with different total energies from $E_0=3$ to 80 keV. Fits through data points are drawn to guide the eye.

of the string potential for channeling [Eq. (2)] and, consequently, of the full three-dimensional atom-surface potential on the atomic species. This dependence can be exploited as a probe for atom-surface potentials. For fast projectiles, the standard method for determining interaction potentials relies on the expansion in terms of binary atom-atom potentials

$$V(\vec{r}) = \sum_j V_j(|\vec{r} - \vec{r}_j|), \quad (4)$$

where $V_j(|\vec{r} - \vec{r}_j|)$ denotes the potential energy of the binary system consisting of the projectile atom (at position \vec{r}) and a free target atom j at position \vec{r}_j . Within this framework, the surface is represented by a cluster of atoms of the topmost surface layers. Established pair potentials used in Eq. (4) are the Moliere,¹⁵ Ziegler-Biersack-Littmark (ZBL),¹⁶ and O'Connor-Biersack (OCB) (Ref. 17) potentials. They are of the functional form

$$V_j(R) = \frac{Z_r Z_p}{R} \sum_i a_i \exp(-b_i R/a_s), \quad (5)$$

where Z_t and Z_p are the nuclear charges of target and projectile atoms, respectively, a_s is a screening length, and the parameter sets $\{a_i\}$ and $\{b_i\}$ characterize the specific potential. The internuclear distance is denoted by R . These potentials are (exponentially) short-ranged and neglect long-range polarization effects. Likewise, they do not account for the transient formation of quasimolecular potential-energy surfaces. For binary atom-atom collisions their applicability is limited to intermediate collision velocities ($v_p \lesssim v_e$) where neither strongly inelastic processes (such as ionization at higher velocities) nor formation of a quasimolecular complex at lower velocities are of importance.^{6,11} This class of potentials is readily available for all pairs of projectile and surface atoms and will serve as point of reference for more advanced potentials.

An element-specific improvement within the framework of binary potentials can be achieved by employing either the Hartree-Fock (HF) approximation or density-functional theory (DFT). Simulations based on HF pair potentials improve the agreement with measured rainbow angles for projectiles near normal incidence^{18,19} as well as grazing incidence.²⁰ The HF pair potentials^{21,22} used in our simulation are based on electron distributions of free atoms which are obtained from electronic wave functions given by Clementi and Roetti.²³ The model used in Ref. 21 takes into account the electrostatic, kinetic, and exchange contributions. The DFT pair potentials are calculated using the ABINIT package.²⁴ The ionic cores are represented by soft pseudopotentials, the Kohn-Sham pseudowave functions are expressed in terms of a plane-wave basis set. We chose for the Al cores structure optimized pseudopotentials²⁵ with the exchange-correlation functional in the generalized gradient approximation (GGA) of Perdew-Burke-Ernzerhof (PBE).²⁶ The DFT pair potential was determined by placing two atoms in a large computing box (supercell) and derived from the forces acting on the atoms.

A comparison of different pair potentials [Eq. (5)], for example, Ar-Al (Fig. 3) shows good agreement for small interatomic distances ($R \lesssim 3$ a.u.) and large values of the repulsive barrier ($V \gtrsim 5$ eV). At larger distances the ZBL potential is more repulsive as compared to the HF and DFT pair potentials. At intermediate distances the OCB potential (dashed line) is even weaker but intersects with the HF and DFT potentials at larger distances. All pair potentials considered here are purely repulsive. Moreover, they are effectively short ranged. Consequently, the sum [Eq. (4)] can be truncated and atoms at distances larger than an appropriate cut-off distance R_{cut} (=10 a.u. in the present simulations) can be neglected. Improvements beyond pure pair potentials of the ZBL or OCB type can be achieved by adding an additional embedding potential V_{emb} .²⁷ This term arises from the shift of the projectile energy levels when embedded in the (unperturbed) electron gas at the surface. Note that V_{emb} can become negative, i.e., attractive for reactive elements. As shown in Ref. 28 this method can improve the agreement

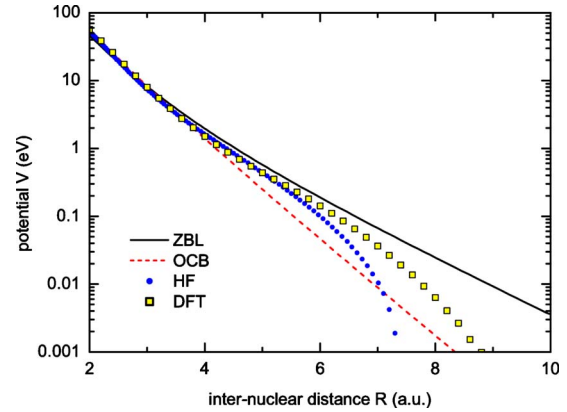


FIG. 3. (Color online) Pair potentials for Ar interacting with Al atoms: OCB (Ref. 17) (dashed curve), ZBL (Ref. 16) (full curve), HF (Ref. 21) (points), and DFT potentials (squares).

between calculated and experimental rainbow angles for some combinations of projectile, target, and channeling direction. A conceptual difficulty in using V_{emb} lies in the proper correction for “double counting” of electronic density which enters both the pair and the embedding potentials.

B. *Ab initio* atom-surface potential

The construction of surface potentials beyond the superposition of atomic pair potentials requires an *ab initio* approach. We calculate the electronic structure of the complex (atom+crystal surface) using the ABINIT code. The combined system is represented by a supercell with periodic boundary conditions of sufficient size in order to avoid interaction of the projectile atom with its replicas in neighboring cells. As we consider neutral atoms, it is sufficient to include laterally four surface unit cells while retaining four crystal layers in order to reduce the numerical effort. Increase in the number of Al layers leads to changes in the force on the projectile by less than 2%. The computational box (supercell) therefore contains 16 Al atoms within the slab and a vacuum layer of 11 crystal layers separating neighboring slabs. As in the case

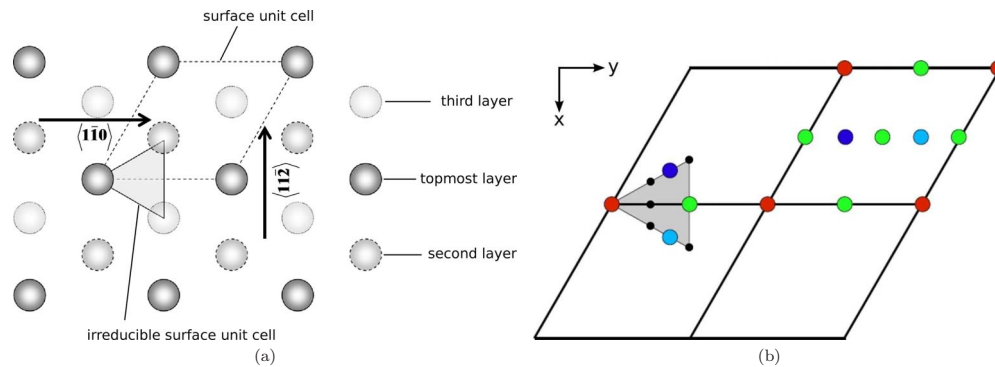


FIG. 4. (Color online) (a) Surface unit cell and channeling directions of the Al(111) surface (topview). Atomic layers are represented by shaded circles. Topmost layer: dark gray with solid circumference; second layer: medium gray with dashed circumference; third layer: light gray with dotted circumference. The surface cell is indicated by the dashed parallelogram, the irreducible cell by the triangle. Two channeling directions are indicated by arrows. (b) Positions (large points) within the irreducible surface unit cell (shaded triangle) required to determine averaged center and edge potentials for the $\langle 1\bar{1}\bar{0} \rangle$ channel of the Ar-Al(111) potential. Equivalent points within the surface unit cell (parallelograms) have same color (shading). Additional grid points at which potentials were calculated are indicated by small black dots.

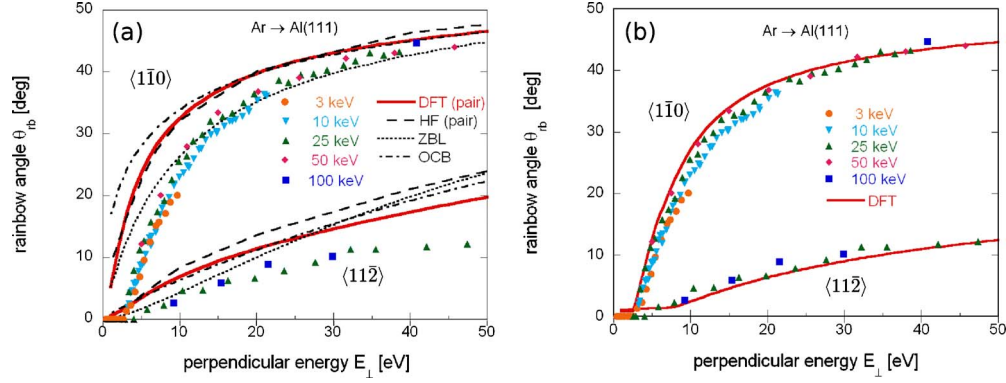


FIG. 5. (Color online) Rainbow angles as function of normal component of kinetic energy, E_{\perp} , for Ar atoms scattered off Al(111) along the $\langle 1\bar{1}0 \rangle$ and $\langle 11\bar{2} \rangle$ directions. Symbols: experimental data for different total kinetic energies E_0 . Curves: results from trajectory simulations based on (a) surface potentials constructed by summation of Ar-Al pair potentials and (b) full Ar-Al(111) potentials from *ab initio* DFT slab calculations.

of pair potentials, we chose for the Al cores structure-optimized pseudopotentials²⁵ with the exchange-correlation functional in the GGA of PBE.²⁶ Within the irreducible surface unit cell we have selected nine lateral positions (large and small circles in Fig. 4) for which the vertical distance of the projectile atom from the topmost layer was varied between 1 and 8 a.u. The potential landscape is thus calculated on a grid with 72 points. Averaging $V(\vec{r})$ at a constant distance z from the topmost atomic layer along the channel direction y results in a two-dimensional string (or channeling) potential $V_{str}(x, z)$ [Eq. (1)]. For computational efficiency of the trajectory simulations with the CTMC method, $V_{str}(x, z)$ was fitted to the functional form

$$V_{str}(x, z) = a(z) + b(z) \cdot \cos\left(\frac{2\pi x}{d}\right) \quad (6)$$

with $a(z)$ and $b(z)$ deduced from the numerically determined potential landscape (see Fig. 4).

It should be stressed that the present *ab initio* calculation provides static (zero-frequency) scattering potentials $V(\omega = 0, \vec{r})$. Dynamical effects such as the finite frequency response when v_{\parallel} becomes comparable to v_e are beyond the scope of the present method. The accuracy of static poten-

tials for scattering at higher kinetic energies E_0 or, equivalently, higher E_{\parallel} is therefore uncertain (see below). Dynamical effects could be, in principle, accounted for by time-dependent DFT (TDDFT). However, the availability of accurate exchange and correlation functional comparable to those for the static case remains an open problem.

V. COMPARISON WITH EXPERIMENT

A. Rare-gas projectiles

He and Ar atoms were scattered off the Al(111) along the $\langle 1\bar{1}0 \rangle$ as well as the $\langle 11\bar{2} \rangle$ channels. Simulations using potentials derived from the summation over pair potentials [see Eq. (4)] yield rainbow angles [Fig. 5(a)] that differ from the experimental data and from the *ab initio* potential simulations [Fig. 5(b)]. Only the *ab initio* potential reproduces the threshold value E_{\perp}^{rb} below which the rainbow angle vanishes. The origin of the failure of pair potentials is the neglect of the contribution of the quasifree-electron gas above the metal surface to the overall interaction potential leading to a systematic overestimation of corrugation at larger distances from the surface ($z \approx 4$ a.u.) (see Fig. 6) where the turning point for energies of E_{\perp}^{rb} is situated. The potential corrugation

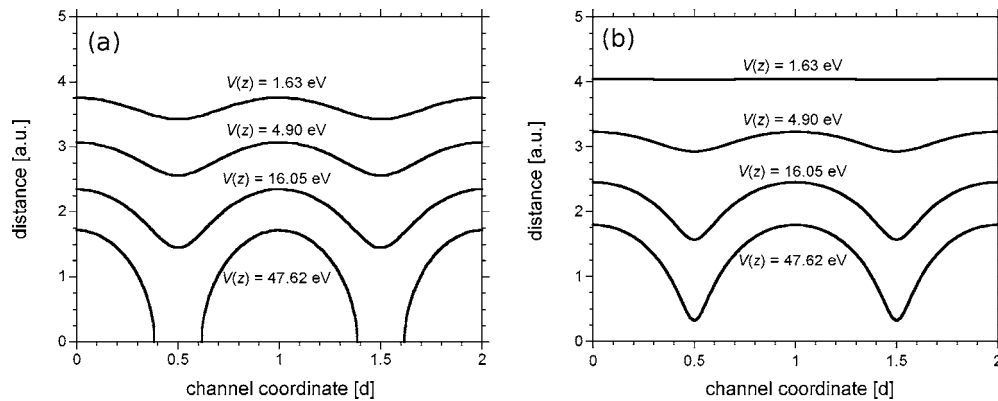


FIG. 6. Isopotential lines of the string potential along the $\langle 1\bar{1}0 \rangle$ direction above an Al(111) surface for Ar. Contours derived from (a) OCB pair potential and (b) *ab initio* DFT slab calculations.

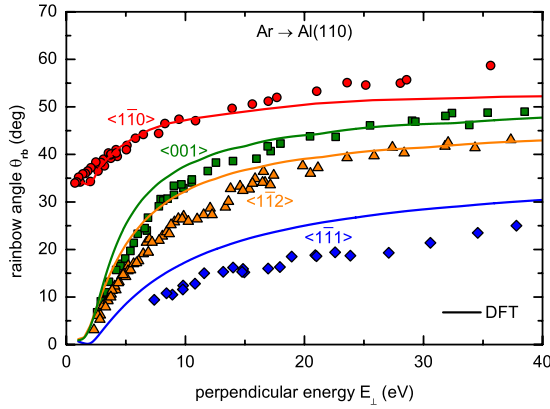


FIG. 7. (Color online) Rainbow angles of Ar atoms scattered from Al(110) along low-indexed directions. Experimental results: solid symbols; simulations using *ab initio* DFT potentials: solid curves.

in the vicinity of the projectiles turning points is crucial for the value of θ_{rb} . Flat potential-energy surfaces near the turning points (small corrugation) lead to small θ_{rb} . While the full projectile-surface *ab initio* calculations yield essentially flat potential surfaces for distances larger than $z \approx 3.5$ a.u. above the topmost atomic layer [Fig. 6(b)], a residual corrugation is found for all pair potentials even up to $z=8$ a.u. resulting in finite rainbow angles down to $E_{\perp}=0$ [Fig. 6(a)]. The monotonic increase in the rainbow angles with increasing E_{\perp} is a direct consequence of the purely repulsive forces acting on a noble gas atom in front of an Al surface. Good agreement is also found for Ar atoms scattered off the (110) face of Al along other low-indexed directions (Fig. 7). The simulated threshold values at low normal energies and the asymptotic value for θ_{rb} agree well with the experiment. The key observation is that even for electronically inert rare-gas projectiles only *ab initio* potentials are accurate enough to reproduce the behavior of $\theta_{rb}(E_{\perp})$ correctly. The rainbow angles for noble gas projectiles scattered off an Al surface are, generally, independent of their total kinetic energy E_0 . For He projectiles scattered off Al(111), however, we observe experimentally a dependence of θ_{rb} on E_0 at constant normal energy E_{\perp} (Fig. 8). Note that this dynamic effect was

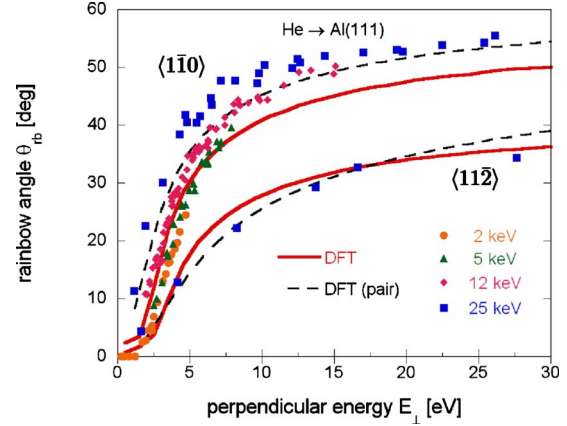


FIG. 8. (Color online) Rainbow scattering angles for He atoms scattered from Al(111) along $\langle 1\bar{1}0 \rangle$ and $\langle 11\bar{2} \rangle$ as indicated. Symbols: experimental results for different total energies as indicated. Curves: results from trajectory simulations based on a full He-Al(111) potential from *ab initio* DFT slab calculations (red, solid line) and surface potentials constructed by summation of He-Al DFT pair potentials (blue, dashed line).

observed for He scattering along the $\langle 1\bar{1}0 \rangle$ channel of Al(111) only. While the calculation using the static full projectile-surface *ab initio* potential agrees well with the data for 2 and 5 keV He projectiles, at higher total energies (12 and 25 keV), the experimental data are in better agreement with calculations using DFT-based pair potentials. Pronounced dynamical effects are plausible since for He at 25 keV the parallel velocity is $v_{\parallel} \approx 0.5v_F$ (v_F : Fermi velocity) so that static potentials may no longer be adequate. By comparison, the highest parallel velocity for argon projectiles ($E_0 = 100$ keV) was only $v \approx 0.3v_F$ (see Fig. 5).

B. Metal atom projectiles

Similar to noble gases the rainbow angles for metal-atom projectiles depend predominantly on E_{\perp} with negligible dependence on E_0 . For metal atoms we mostly find finite values of θ_{rb} for $E_{\perp} \rightarrow 0$ due to attractive regions in the surface potential (see Fig. 9), whereas the purely repulsive potentials

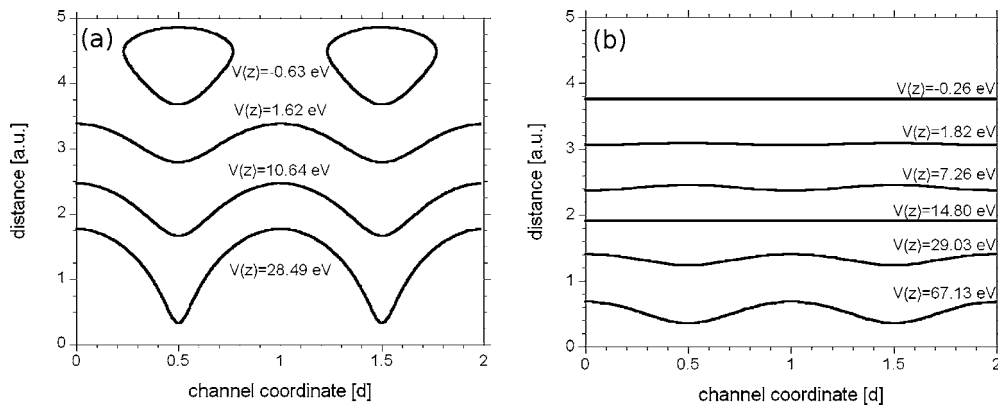


FIG. 9. Isopotential lines of the channel potential along the (a) $\langle 1\bar{1}0 \rangle$ and (b) the $\langle 11\bar{2} \rangle$ directions above an Al(111) surface as seen by an impinging Al atom.

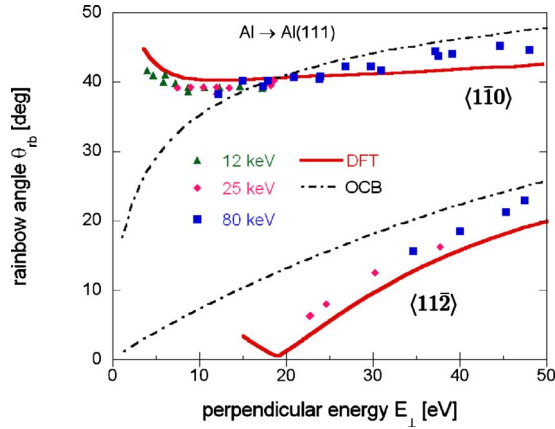


FIG. 10. (Color online) Rainbow angles of Al atoms scattered off an Al(111) surface along the $\langle 1\bar{1}0 \rangle$ and $\langle 11\bar{2} \rangle$ directions. Symbols: experimental results for different total energies E_0 , black dashed lines: simulations using the OCB potential, and red solid curves: simulations based on complete Al-Al(111) *ab initio* DFT surface potentials.

for noble gas atoms lead to vanishing rainbow angles at $E_{\perp}=0$. The attractive forces of the surface potential for alkali and metal atoms enhance the complexity of the problem compared to noble gas atoms.

Simulations of rainbow scattering of Al atoms impinging on the Al(111) surface underline the importance of accurate potentials. We find a completely different dependence of θ_{rb} on E_{\perp} for the $\langle 1\bar{1}0 \rangle$ and $\langle 11\bar{2} \rangle$ channels (Fig. 10). For the latter direction $\theta_{rb}(E_{\perp})$ is much smaller and displays a zero near $E_{\perp}=19$ eV and an increase at lower E_{\perp} . For the $\langle 1\bar{1}0 \rangle$ direction θ_{rb} is almost independent of E_{\perp} and remains nearly constant at $\sim 40^\circ$ with only a slight increase below $E_{\perp} \approx 10$ eV.

While conventional pair potentials (e.g., OCB) fail to even qualitatively reproduce this behavior, potentials from *ab initio* DFT calculations succeed to model the strong corrugation in the wide $\langle 1\bar{1}0 \rangle$ channel [Fig. 9(a)] resulting in large rainbow angles. The vanishing corrugation above the narrow $\langle 11\bar{2} \rangle$ channel [Fig. 9(b)] leads to the zero of θ_{rb} at $E_{\perp}=19$ eV (corresponding to $z_c \approx 1.9$). This, however, does not indicate a threshold behavior as our simulations indicate finite values $\theta_{rb} > 0$ also for smaller E_{\perp} . Rather, at a distance of $z_c \approx 1.9$ a.u. [see Fig. 9(b)] the corrugation changes sign with a vanishing corrugation at the transition giving rise to the zero in θ_{rb} . Similar shifted corrugations were also found in *ab initio* calculations for He atoms in front of Cu and Al surfaces²⁹ without, however, a transition from one regime to the other.

Since pair potentials such as ZBL, OCB [Eq. (5)] depend on the nuclear charges only, they cannot account for the electronic rearrangement near the metal surface and are, therefore, inadequate to model the dependence of θ_{rb} on E_{\perp} . As an example for projectile-specific electronic rearrangement we compare the electron densities of an Al and an Ar atom placed in front of an Al(111) surface (see Fig. 11). As the Al projectile approaches the surface, formation of quasimolecular electronic orbitals sets in and projectile electrons become

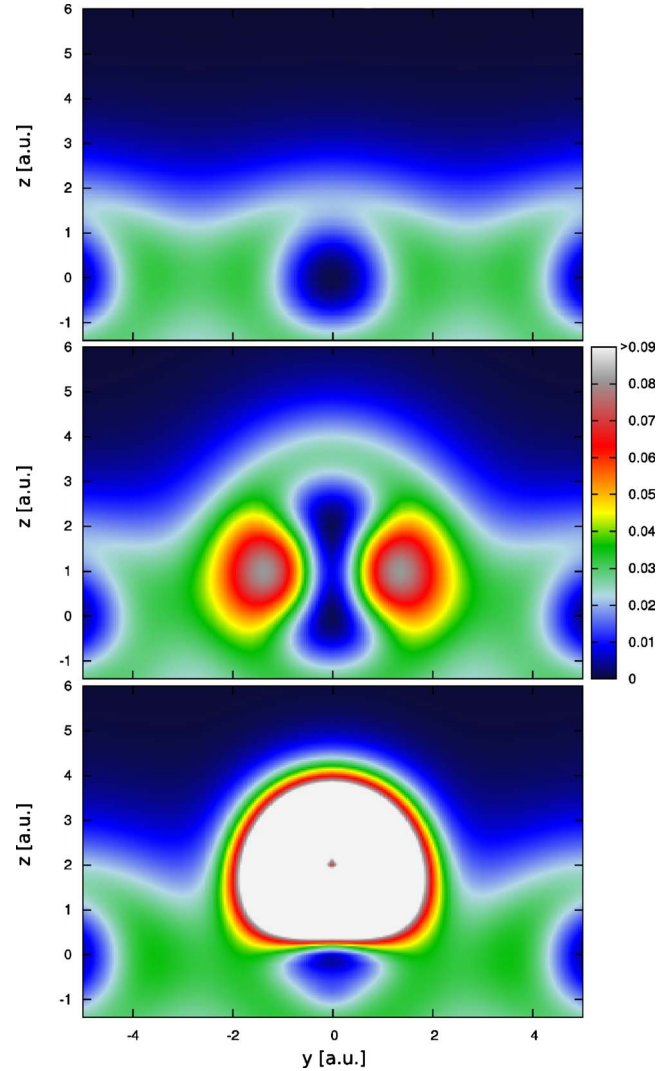


FIG. 11. (Color online) Electron density near an unperturbed Al(111) surface (upper panel) and perturbed by the presence of an Al (mid panel) and by an Ar atom (lower panel) located 2 a.u. above a surface atom. Only electrons from the outermost atomic shells are explicitly included.

increasingly integrated into the crystal electronic structure, i.e., these electrons become part of the target electron gas. Instead of a spherically symmetric atomic electron-density distribution, the highest electron density is observed in a torus between projectile and target atom. The middle panel of Fig. 11 shows a perpendicular cut through this torus which lies parallel to the surface plane. On the other hand, inert Ar projectiles (bottom panel in Fig. 11) retain a typical atomic electron density and are only slightly deformed by the presence of the target surface.

C. Rainbows for atoms with large electron affinities

For projectiles from the main groups V, VI, and VII of the periodic table characterized by large electron affinities, the energy dependence of θ_{rb} differs significantly from the previously discussed cases.³⁰ θ_{rb} strongly depends on E_{\parallel} at fixed E_{\perp} as shown for N scattered off Al(111) in Fig. 12. The

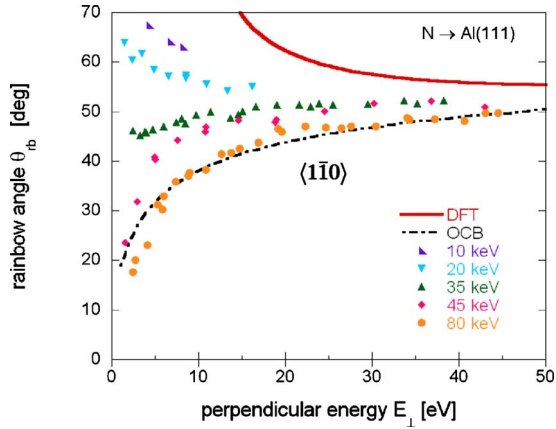


FIG. 12. (Color online) Rainbow angles of N atoms scattered off an Al(111) surface along the $\langle 1\bar{1}0 \rangle$ direction. Symbols: experimental data for different total energies, black dashed lines: simulation using the OCB potential, red solid curves: simulation based on N-Al(111) *ab initio* DFT surface potentials.

experimental data lie in between the *ab initio* DFT prediction and the pair potential (OCB) approximation.

For small kinetic energies ($E_0 \lesssim 10$ keV) the experiment is closer to the DFT result and for higher energies ($E_0 = 80$ keV) it is close to the OCB curve. Qualitatively, this behavior can be understood in terms of the smaller electronic orbital velocity of the affinity level, v_{orb} . The projectile velocity becomes comparable to v_{orb} at smaller E_0 than for rare-gas or metal atoms. Consequently, the attractive force decreases with increasing E_0 since the electronic polarization can no longer adiabatically follow the projectile. This renders the interaction more noble gaslike. Apparently, *ab initio* DFT and phenomenological OCB pair potentials represent limiting cases of small and large E_0 , respectively. In the latter case, the rearrangement of the electron density is expected to become negligible.

VI. ANALYSIS OF THE ADIABATIC ELECTRONIC RESPONSE

In order to analyze the origin of the element-specific variations in the static atom-surface potential, we have investigated the adiabatic electronic response for three prototypical cases: a rare gas (Ne), an alkali atom (Na), and a high-affinity halide (F). These elements are next to each other in the periodic table with minimal variation of Z_p and, thus, of standard pair potentials such as ZBL or OCB. For each of these atomic species we analyze the electronic response in terms of the electron-localization function (ELF) (Refs. 31–33) and perform a Bader analysis^{34,35} of the system formed by the projectile and the Al(111) surface. The ELF is, in essence, a measure for the Pauli repulsion. Starting from the Hartree-Fock conditional pair probability for finding an electron at \vec{r}' when another electron with the same spin is located at \vec{r} , Becke and Edgecombe³¹ designed a scalar function (ELF) ranging from zero to one that visualizes chemical bonding. Values close to one indicate complete expulsions of electrons of the *same* spin orientation from the vicinity of

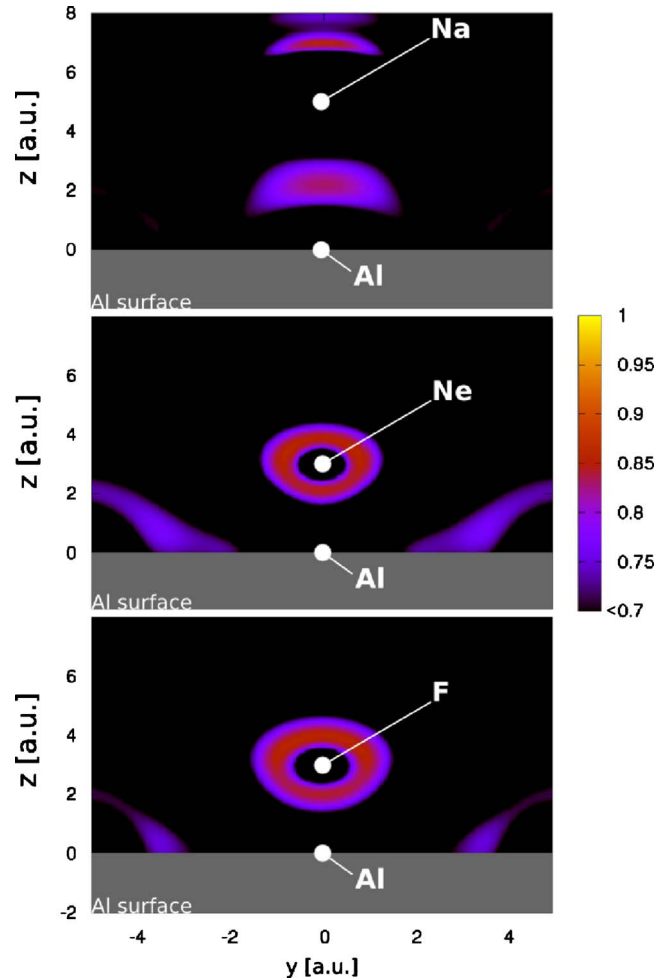


FIG. 13. (Color online) Cut through ELFs for (top panel) Na projectiles at $z=5$ a.u. (mid panel) Ne and (bottom panel) F projectiles at $z=3$ a.u. above a surface atom of an Al(111) surface. The nearest-neighbor distance of the Al surface atoms (on the y axis) is ≈ 5.411 a.u.

another electron. A prototypical case for this limit would be the formation of a bond or of lone electron pairs. In a homogeneous electron gas, $\text{ELF}=0.5$. Small values of the ELF are typical for regions between different electron shells. The Bader analysis, in turn, allows one to determine the number of electrons associated with a specific atom within the quasimolecule by investigating the topography of the electron density and/or its derivative. These analytical tools characterize the type and degree of bonding between the surface and the projectile atom (for a review see Ref. 33). The resulting change in potential energies is responsible for the observed variations in scattering distributions, in particular, in the rainbow angle.

The ELF (only the valence electrons are included) of the noble gas Ne shows (Fig. 13) a spherical structure, i.e., the hardly perturbed valence electron shell without bonding to the surface. The ELF of F at the same distance ($z=3$ a.u.) resembles that of Ne with the spherical shell slightly expanded. The number of electrons attached or detached from the projectile, ΔN , as deduced from the Bader analysis ($\Delta N = \text{number of electrons} - Z_p$), provides a simple explanation

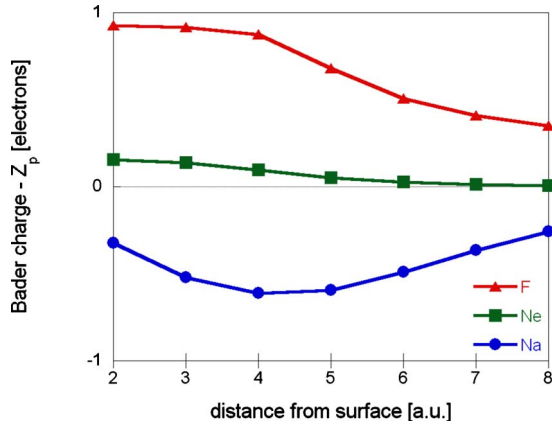


FIG. 14. (Color online) Number of electrons attached (positive)/detached (negative) to/from the projectiles F, Ne, and Na at different distances above an atom of the topmost Al(111) surface layer (Bader charge states $-Z_p$).

tion (Fig. 14): an electron is almost completely transferred to F, transiently forming F^- at $z=3$ a.u. close to the equilibrium position of an F adatom in front of Al(111) according to our DFT calculations. While the closed-shell structure for Ne indicates the absence of bonding and a purely repulsive interacting potential, the similar closed-shell structure for F^- implies a strong transient ionic bonding and regions of an attractive potential causing the nonmonotonic behavior of $\theta_{rb}(E_\perp)$.

The valence electron of Na, on the other hand, is partially detached from the projectile (Fig. 14). This is consistent with an earlier analysis of the Na-Al(111) system³⁶ where the apparent “invisibility” of Na atoms on Al surfaces in scanning tunnel microscope images was associated with the electron transfer from the sodium atom. The ELF for Na at a distance of $z=5$ a.u. (Fig. 13) above an Al surface atom displays high values in the region between the two atoms significantly exceeding the metallic value of 0.5. While a purely metallic bond can be ruled out, the substantial charge-transfer points to a transient polar bond. The time scale for such a metallic polarization is apparently shorter than for the formation of F^- . Consequently, the approximate validity of the adiabatic potential-energy surface extends for metallic projectiles to higher parallel velocities v_\parallel than for high-electron affinity

projectiles, resulting in a weak E_0 dependence for metals but stronger variations for halides and elements from the groups V and VI.

VII. PLANAR CHANNELING POTENTIALS

We have also investigated the differences between an *ab initio* approach and the pair potential method for planar channeling, i.e., for scattering along high-indexed (random) directions. The resulting potential $V_{planar}(z)$ represents an average over the surface plane and depends on the distance z to the surface only [see Eq. (3)].

Figure 15 shows a comparison of the OCB and ZBL potentials with *ab initio* potentials for Ar atoms incident on Al(111) and Al(110) surfaces. For small projectile-surface distances ($z < 2.5$ a.u.) the potentials closely agree with each other. For larger distances our *ab initio* potential lies in between the averaged pair potentials which differ from each other by an order of magnitude at $z=8$ a.u. For small distances from the surface (or $E_\perp \gtrsim 10$ eV), ZBL or OCB potentials might be reasonable choices. However, even for rare-gas projectiles, these potentials fail at intermediate distances $z \gtrsim 3$ a.u. and cannot account for the electronic structure of the different crystal faces. For other projectile species, the failure of OCB and ZBL potentials is even more obvious because of the lack of attractive forces between projectile and surface. Therefore, *ab initio* calculations are needed. A first-order correction to planar averaged pair potentials can be introduced with embedding potentials which take into account polarization effects.²⁷

VIII. CONCLUSIONS

We have presented a joint experimental and theoretical study of atom-surface potentials probed by rainbow scattering for axial surface channeling at different crystal faces and different groups of atomic projectiles. For low perpendicular energies ($E_\perp \approx 10$ eV) and total kinetic energies ($E_0 \approx 1$ keV/amu) such that the adiabatic limit of potential surfaces applies, we have shown that conventional pair potentials fail to reproduce several characteristic trends of our experimental data. *Ab initio* calculations of the combined collisional complex of atom plus Al surface are required to

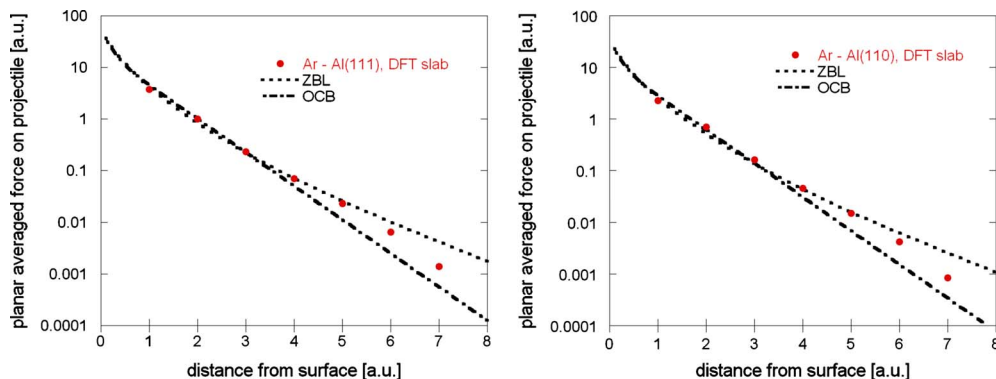


FIG. 15. (Color online) Planar-averaged projectile-surface potentials for Ar atoms incident on (left panel) Al(111) and (right panel) Al(110) surfaces as a function of the distance from surface.

achieve good agreement of classical-trajectory Monte Carlo scattering simulations with experimental data. At high (parallel) projectile energies the onset of nonadiabatic effects can be observed. For atoms with large electron affinities and transient negative-ion formation, the breakdown of the adiabatic approximation following of electronic polarization sets in at energies $E_0 \approx 1$ keV/amu while for rare gases deviations become noticeable at $E_0 \approx 5$ keV/amu. These dynamic effects cannot be modeled by the present method, as potential calculations refer the limit of $E_0 \rightarrow 0$. Investigation of such dynamical effects in terms of effective surface potentials via TDDFT is an interesting topic for future investigations.

ACKNOWLEDGMENTS

We thank Konrad Gärtner, Friedrich-Schiller-Universität Jena, for providing HF potentials. The assistance of S. Wethekam and K. Maass in the preparation of the experiments is gratefully acknowledged. This work was supported by DFG (Proj. Wi 1336), the Austrian Fonds zur Förderung der wissenschaftlichen Forschung (Projects SFB41 VICOM, No. 17449 and No. 17359), and the TeT under Grant No. AT-7/2007. One of us (K.T.) was also partially supported by the grant Bolyai from the Hungarian Academy of Sciences and the Hungarian National Office for Research and Technology.

-
- ¹O. Stern, *Naturwiss.* **17**, 391 (1929); I. Estermann and O. Stern, *Z. Phys.* **61**, 95 (1930).
- ²D. Farias and K. H. Rieder, *Rep. Prog. Phys.* **61**, 1575 (1998).
- ³*Helium Atom Scattering from Surfaces*, edited by E. Hulpke (Springer-Verlag, Berlin, 1982).
- ⁴J. P. Toennies, *Appl. Phys.* **3**, 91 (1974).
- ⁵H. Winter, *Phys. Rep.* **367**, 387 (2002); H. Winter, *J. Phys.: Condens. Matter* **8**, 10149 (1996).
- ⁶J. Burgdörfer, in *Review of Fundamental Processes and Applications of Atoms and Ions*, edited by C. D. Lin (World Scientific, Singapore, 1993), p. 517.
- ⁷D. S. Gemmell, *Rev. Mod. Phys.* **46**, 129 (1974).
- ⁸A. Schüller, S. Wethekam, and H. Winter, *Phys. Rev. Lett.* **98**, 016103 (2007); A. Schüller and H. Winter, *ibid.* **100**, 097602 (2008).
- ⁹P. Rousseau, H. Khemliche, A. G. Borisov, and P. Roncin, *Phys. Rev. Lett.* **98**, 016104 (2007).
- ¹⁰F. Aigner, N. Simonović, B. Solleder, L. Wirtz, and J. Burgdörfer, *Phys. Rev. Lett.* **101**, 253201 (2008).
- ¹¹J. Burgdörfer and C. Lemell, in *Slow Heavy-Particle Induced Electron Emission from Solid Surfaces*, Springer Tracts in Modern Physics Vol. 225 (Springer Berlin, Heidelberg, 2007), pp. 1–38.
- ¹²A. W. Kleyn and T. C. M. Horn, *Phys. Rep.* **199**, 191 (1991), and references therein.
- ¹³S. Wethekam and H. Winter, *Nucl. Instrum. Methods Phys. Res. B* **258**, 48 (2007).
- ¹⁴D. Danailov, J. H. Rechten, and K. J. Snowdon, *Surf. Sci.* **259**, 359 (1991).
- ¹⁵G. Molière, *Z. Naturforsch. A* **2**, 133 (1947).
- ¹⁶J. F. Ziegler, J. P. Biersack, and U. Littmark, *The Stopping and Ranges of Ions in Solids* (Pergamon Press, New York, 1985).
- ¹⁷D. J. O'Connor and J. P. Biersack, *Nucl. Instrum. Methods Phys. Res. B* **15**, 14 (1986).
- ¹⁸A. D. Tenner, R. P. Saxon, K. T. Gillen, D. E. Harrison, Jr., T. C. M. Horn, and A. W. Kleyn, *Surf. Sci.* **172**, 121 (1986).
- ¹⁹C. A. DiRubio, R. L. McEachern, J. G. McLean, and B. H. Cooper, *Phys. Rev. B* **54**, 8862 (1996).
- ²⁰A. Schüller, S. Wethekam, A. Mertens, K. Maass, H. Winter, and K. Gärtner, *Nucl. Instrum. Methods Phys. Res. B* **230**, 172 (2005).
- ²¹K. Gärtner and K. Hehl, *Phys. Status Solidi B* **94**, 231 (1979).
- ²²K. Gärtner (private communication).
- ²³E. Clementi and C. Roetti, *At. Data Nucl. Data Tables* **14**, 177 (1974).
- ²⁴X. Gonze, J. M. Beuken, R. Caracas, F. Detraux, M. Fuchs, G. M. Rignanese, L. Sindic, M. Verstraete, G. Zerah, F. Jollet, M. Torrent, A. Roy, M. Mikami, Ph. Ghosez, J.-Y. Raty, and D. C. Allanet, *Comput. Mater. Sci.* **25**, 478 (2002).
- ²⁵A. M. Rappe, K. M. Rabe, E. Kaxiras, and J. D. Joannopoulos, *Phys. Rev. B* **41**, 1227 (1990); **44**, 13175(E) (1991); <http://www.sas.upenn.edu/rappegroup/>
- ²⁶J. P. Perdew, K. Burke, and M. Ernzerhof, *Phys. Rev. Lett.* **77**, 3865 (1996).
- ²⁷M. J. Puska and R. M. Nieminen, *Phys. Rev. B* **43**, 12221 (1991).
- ²⁸A. Schüller and H. Winter, *Nucl. Instrum. Methods Phys. Res. B* **256**, 122 (2007).
- ²⁹N. Jean, M. I. Trioni, G. P. Brivio, and V. Bortolani, *Phys. Rev. Lett.* **92**, 013201 (2004).
- ³⁰A. Schüller and H. Winter, *Nucl. Instrum. Methods Phys. Res. B* **267**, 2621 (2009).
- ³¹A. D. Becke and K. E. Edgecombe, *J. Chem. Phys.* **92**, 5397 (1990).
- ³²A. Savin, O. Jepsen, J. Flad, O. K. Andersen, H. Preuss, and H. G. von Schnering, *Angew. Chem., Int. Ed. Engl.* **31**, 187 (1992).
- ³³A. Savin, R. Nesper, S. Wengert, and T. F. Fässler, *Angew. Chem., Int. Ed. Engl.* **36**, 1808 (1997).
- ³⁴R. F. W. Bader, *Atoms in Molecules: A Quantum Theory* (Clarendon Press, Oxford, 1994).
- ³⁵R. F. W. Bader, *J. Phys. Chem. A* **102**, 7314 (1998).
- ³⁶F. Máca, *Surf. Interface Anal.* **27**, 555 (1999).